TABLE 1. Characterization of (1,2-Diaminocyclohexane)platinum(II) (DACHPt)-Loaded Micelles

micelles	cRGD[a,e] (%)	cRAD[a,f] (%)	size[b] (nm)	PDI[b,g]	[Pt]/[COO][c] (mol/mol)	zeta potential[d] (mV)
ctrl/m[h]	0	0	27	0.096	0.51	−3.1 ± 0.5
5% cRGD/m[i]	5 ± 2	0	28	0.088	0.50	−3.4 ± 0.3
10% cRGD/m	10 ± 2	0	30	0.100	0.55	−2.8 ± 0.7
20% cRGD/m	22 ± 2	0	29	0.099	0.52	−2.3 ± 0.4
40% cRGD/m	43 ± 2	0	31	0.093	0.49	−2.9 ± 0.3
20% cRAD/m[j]	0	20 ± 2	31	0.101	0.54	−2.5 ± 0.7

[a] Determined by ^{1}H NMR. [b] Determined by DLS. [c] Determined based on ICP-MS measurements of platinum concentration and the weight of dried micelles. [d] Determined by laser Doppler electrophoresis (n = 4, mean ± SD). [e] cRGD, cyclic Arg-Gly-Asp. [f] cRAD, cyclic Arg-Ala-Asp. [g] PDI, polydispersity. [h] ctrl/m, control DACHPt/m. [i] cRGD/m, cRGD-linked DACHPt/m. [j] cRAD/m, cRAD-linked DACHPt/m.

alkali conditions to obtain N_3-PEG-*b*-P(Glu). The α-end azido group of N_3-PEG-*b*-P(Glu) was then reduced to a primary amino group and reacted further with *N*-(4-maleimidobutyryloxy)sulfosuccinimide (sulfo-GMBS) to obtain Mal-PEG-*b*-P(Glu) (Supporting Information Figure S1). By controlling the ratio of MeO-PEG-*b*-P(Glu)/Mal-PEG-*b*-P(Glu), a series of surface-tunable micelles with different percentages of maleimide groups on their surfaces was prepared before cyclo[RGDfK(CX-)] (cRGD peptide, X = 6-aminocaproic acid, ε-Acp) was introduced onto the DACHPt/m surface *via* Michael addition reactions. This strategy facilitated the preparation of DACHPt micelles with 5−40% cRGD ligands (Table 1). These percentages, which represent the molarities of ligand molecules on the DACHPt/m surface, were determined by ^{1}H nuclear magnetic resonance (NMR) spectroscopy (Supporting Information).

Cyclo[RADfK(CX-)] (cRAD peptide, X = ε-Acp) was also used as a nontargeting ligand molecule. As described in detail later, 20% cRGD-linked DACHPt/m had the best potential for *in vitro* activity. Thus, we prepared 20% cRAD-linked DACHPt/m as a nontargeting-ligand-linked micelle, which was used as a control micelle for comparison. In all cases, the ligand-linked micelles prepared in this study had similar characteristics (Table 1). Even after modifying the surface, all the micelles produced had diameters between 27 and 31 nm with narrow polydispersity (PDI). Therefore, it was appropriate to verify the effect of ligands by using these micelles.

Integrin-Dependent Activity of Ligand-Linked DACHPt/m in Tumor Cells. To evaluate the biological activities of the ligand-linked micelles, we quantitatively analyzed their cellular uptake in $\alpha_v\beta_3$- and $\alpha_v\beta_5$-positive U87MG human GBM cells by inductively coupled plasma mass spectrometry (ICP-MS) (Figure 2a). Free oxaliplatin was taken up continuously by the U87MG cells, whereas control DACHPt/m (ctrl/m, without ligand molecules) was internalized slowly *via* endocytosis.[36] In contrast, higher cellular uptake of cRGD/m was observed in the early stages of the experiment, particularly when the amount of cRGD was increased (Figure 2a). With 20% and 40% cRGD/m, the internalized platinum amount was approximately 2.5-fold higher than that with 20% cRAD-linked DACHPt/m (20% cRAD/m) after 3 h incubation (Figure 2a). Thus, we prepared a fluorescence (Alexa 555)-labeled PM (Supporting Information) to perform *in vitro* confocal laser scanning microscopy (CLSM). The results showed that the 20% cRGD/m was taken up rapidly into the U87MG cells, whereas the ctrl/m and 20% cRAD/m were internalized more gradually (Figure 2b). On the basis of the CLSM images, the quantification of cell-associated fluorescence was consistent with the ICP-MS data (Figure 2c). As shown in Figure 3a, the introduction of cRGD ligands increased the *in vitro* cytotoxicity of DACHPt/m. The results obtained 48 h after incubation (white bar in Figure 3a) showed that 50% growth inhibitory concentration (IC_{50}) values were lower with 20% and 40% cRGD/m. Due to the cRGD-associated cellular uptakes (Figure 2a), this tendency was enhanced when the cytotoxicity assay method was changed to a 3 h drug/micelle exposure, followed by 48 h postincubation (gray bar in Figure 3a). These results suggested that the ligand density was essential for increasing the cytotoxicity of micelles. To confirm the recognition of integrins by the cRGD ligand, we established α_v integrin downregulated U87MG cells by RNA silencing (Supporting Information Figure S2a and b). Flow cytometric analysis revealed that the U87MG cells expressed $\alpha_v\beta_3$ (blue line) and $\alpha_v\beta_5$ (red line) integrins, whereas the α_v integrin-downregulated U87MG cells expressed almost no $\alpha_v\beta_3$ and $\alpha_v\beta_5$ integrins (Figure 4a and b). *In vitro* cytotoxicity assays using integrin-downregulated U87MG cells showed that the activity of cRGD/m was changed to similar values of both ctrl/m and 20% cRAD/m, thereby indicating a crucial role for binding of cRGD ligands with the $\alpha_v\beta_3$ and $\alpha_v\beta_5$ integrins in the enhanced cytotoxicity of cRGD/m against the U87MG cells (Figure 3b). It should be noted that the recently developed antiangiogenesis drug cilengitide includes a cRGD sequence and has been demonstrated to have antitumor activity against GBM.[30,31,41−45] However, the cytotoxicity of cilengitide itself is very low. For instance, Mikkelsen *et al.* studied the cytotoxicity of cilengitide in combination with X-ray irradiation, but no significant cytotoxicity was observed for 10 μM cilengitide without radiation.[44] In our system, only 2 μM cRGD (in the case of 40% cRGD-linked DACHPt/m solution) is

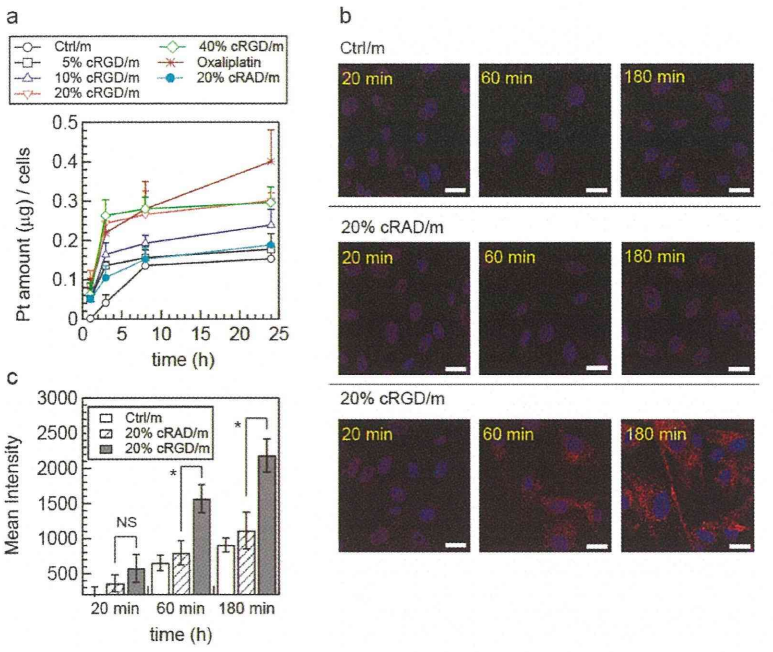

Figure 2. Cellular uptake of DACHPt/m with various ligand species and densities. (a) *In vitro* cellular uptake of micelle-encapsulated platinum, which was determined by ICP-MS. The obtained cell-associated platinum increased as the percentage ligand payload in the micelles increased, whereas ctrl/m remained at low values. Experiments were performed four times in quadruplicate. They produced similar results. Bars represent the mean ± standard error of the mean (SEM). (b) *In vitro* CLSM of Alexa 555-labeled ctrl/m, 20% cRGD/m, and 20% cRAD/m uptake in U87MG glioblastoma cells. The cells were incubated with the respective micelle solutions (10 μM platinum) for 20, 60, and 180 min at 37 °C. All pictures show merged images, which include the nuclei (blue) and micelles (red). Scale bars represent 20 μm in all images. (c) Quantitative analysis of the amount of internalized micelles based on the CLSM results. Thirty different cells were analyzed and evaluated at each time point. Data represent mean ± SEM from three independent experiments performed in triplicate. The data were analyzed using Student's *t*-test, and *$p < 0.001$ was considered significant.

included in 100 μM (based on DACHPt) micelle solution. Thus, the concentrations of cRGD in our micelle did not reach a toxic range. Overall, these results highlight the importance of the ligand density, particularly when the surface payload of peptide ligand molecules on the micelle reached 20–40%, which correlated with the maximum cancer cell uptake and cytotoxicity.

Therapeutic Efficacy and Accumulation Behavior of Ligand-Linked DACHPt/m in Human GBM Models. U87MG tumors have a highly angiogenic vasculature and overexpress integrin receptors, as described above. Thus, our ligand-linked micelle system should be highly suitable for the treatment of GBM models. On the basis of the results of *in vitro* cytotoxicity assays, 20% cRGD ligand-linked DACHPt/m was tested against xenografted U87MG tumor-bearing mice and compared with oxaliplatin and 20% cRAD/m. These mice were treated by systemic injections of micelle solutions every other day (total of three injections), starting 5 days after tumor inoculation. While no inhibition of tumor growth was observed in oxaliplatin-treated tumors (Figure 5a), 20% cRGD-linked micelles demonstrated significant tumor growth inhibition (Figure 5a). Conversely, nontargeting-ligand-linked micelle, cRAD/m, had no therapeutic effect, indicating the sequence specificity of the peptide ligand was essential (Figure 5a). According to previous reports, single-cilengitide treatments with a high dosage of cRGD, such as 2400 mg/m^2, against brain tumor have provided only moderate therapeutic efficacy.[45] Therefore, the antitumor activity that we showed in this study is assumed to be caused by the incorporated DACHPt, not by cRGD. The interesting point here is the tumor-accumulating behavior of cRGD/m, as it revealed a fast accumulation within 4 h after administration (Figure 5b, *ca.* 2.2-fold at 4 h *vs* 20% cRAD/m), followed by the further gradual accumulation until 24 h, despite both micelles showing similar size (Table 1) and comparable blood circulation profiles (Figure 5c). Thus, the tumor-association behavior of cRGD/m is clearly distinct from micelles that can be accumulated into tumors just by the EPR effect, indicating the key features of ligand effects.

To understand the functionality of cRGD/m in a human GBM model, the *in vivo* behaviors of cRGD/m and cRAD/m were comparatively analyzed by IVCLSM. As we reported previously, IVCLSM is a useful technique to reveal blood circulation, extravasation, and tissue penetration of micelles in living animals.[37] Here, cRGD/m and cRAD/m were labeled with Alexa 647 (red) and DyLight 488 (green) fluorescent probes, respectively (Supporting Information), and concurrently injected iv into the U87MG tumor-bearing mice. In this

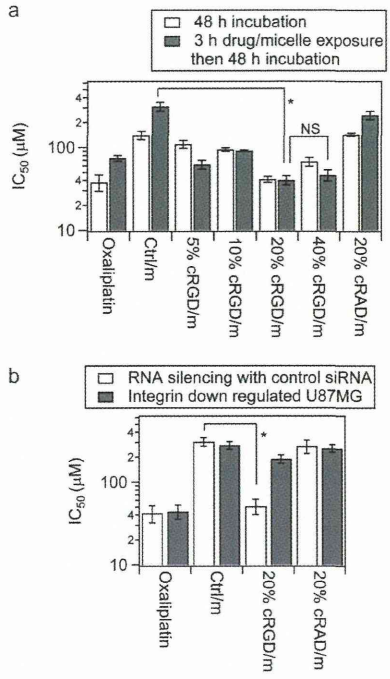

Figure 3. Variation in IC_{50} values with U87MG *in vitro* treatment. (a) *In vitro* cytotoxicities of free oxaliplatin or DACHPt/m with different percentages of ligand molecules in the U87MG cells and (b) *in vitro* cytotoxicities of oxaliplatin, 20% cRGD/m, and 20% cRAD/m in α_v integrin-downregulated U87MG cells (Supporting Information). The IC_{50} values were determined using Cell Counting Kit-8 and are expressed as the percentages of control wells. The experiments were confirmed four times. The data were analyzed using Student's *t*-test, and *$p < 0.001$ was considered significant.

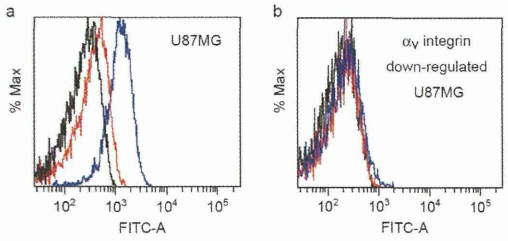

Figure 4. Flow cytometric analysis of integrin expression. (a) U87MG glioblastoma cells and (b) α_v integrin-down-regulated U87MG cells. FITC-labeled mouse IgG: control, black; FITC-labeled anti-$\alpha_v\beta_3$ integrin antibody: blue; and FITC-labeled anti-$\alpha_v\beta_5$ integrin antibody: red.

case, it is possible to evaluate the real-time extravasation and penetration of the micelles based on the changes in fluorescence signals within the same tumor. Figure 6a and b show IVCLSM snapshots of the U87MG tumor site. At 5 min after administration, the color in the bloodstream appeared yellow due to the co-localization of both micelles (Figure 6a). At 5 h after injection, the fluorescence signal corresponding to cRGD/m (red) was clearly observed inside the tumor tissue (Figure 6b). This phenomenon was confirmed by using the opposite combination of fluorescent probes, *i.e.*, DyLight 488-labeled cRGD/m (green) and Alexa

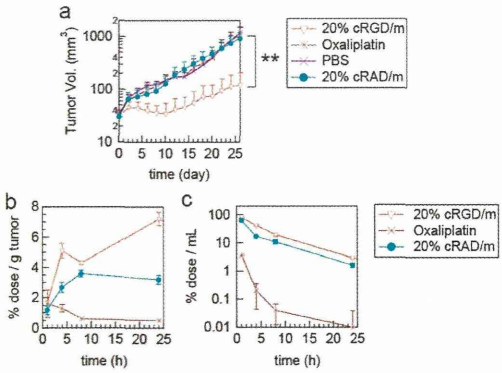

Figure 5. *In vivo* anticancer activity, plasma clearance, and tumor accumulation of cRGD- and cRAD-linked DACHPt/m. (a) Comparison of tumor growth inhibition with cRGD/m and cRAD/m. Five days after tumor cell transplantation, the mice were injected intravenously with micelles. The micelles (4 mg/kg based on DACHPt) were administered every other day (three injections). Oxaliplatin was used as a control platinum drug (dose = 8 mg/kg) with the same treatment schedule. Bars represent mean ± SD (n = 8). Two-way ANOVA was used to analyze the differences in the tumor mass volume, and **$p < 0.001$ was considered significant. (b) Tumor accumulation of DACHPt/m and oxaliplatin. Mice bearing U87MG tumors (n = 6) were injected intravenously with 20% cRGD/m, 20% cRAD/m, and oxaliplatin at 100 μg/mouse on a DACHPt basis. The mice were sacrificed 1, 4, 8, and 24 h after injection. Acid digestion of all tumors was performed using approximately 1.0 mL of concentrated HNO_3 at 200 °C, and the dried samples were dissolved in 1 vol % HNO_3(aq) (1.0 mL). Platinum concentration was measured by ICP-MS. Bars represent mean ± SEM. (c) Plasma clearance of DACHPt/m and oxaliplatin. Blood was collected from the inferior vena cava, heparinized, and centrifuged to obtain the plasma. Acid digestion of all samples was performed using approximately 1.0 mL of concentrated HNO_3 at 200 °C, and the dried samples were dissolved in 1 vol % HNO_3(aq) (1.0 mL). Platinum concentration was measured by ICP-MS. Data represent mean ± SEM (n = 6).

647-labeled cRAD/m (red), and the result indicated the time-dependent increase in the green fluorescence (cRGD/m) at tumor tissue (Figure 6c,d and Supporting Video). To quantitatively evaluate the accumulation of the micelles at the tumor tissue, three different regions were selected (white rectangle in Figure 6c), and the changes in the fluorescence signals were analyzed for up to 9 h. For cRGD/m, a rapid increase in the fluorescence signals (green) in the tumor tissue during the initial 5 h was confirmed (Figure 6e). This observation is well consistent with the ICP-MS results of the tumor accumulation as shown in Figure 5b. Thus, the IVCLSM results indicated that despite the subtle difference in the amino acid sequence, the cRAD peptides were unable to facilitate extravasation and penetration of PMs as could cRGD. Moreover, based on the IVCLSM results (Figure 6c and d), we quantitatively analyzed the permeability of DyLight 488-labeled cRGD/m and Alexa 647-labeled cRAD/m from vasculature to the interstitium of U87MG tumor. The fluorescence intensity in the selected region (blue rectangle in Figure 6c) was observed. As shown in Figure 6f, the strong green

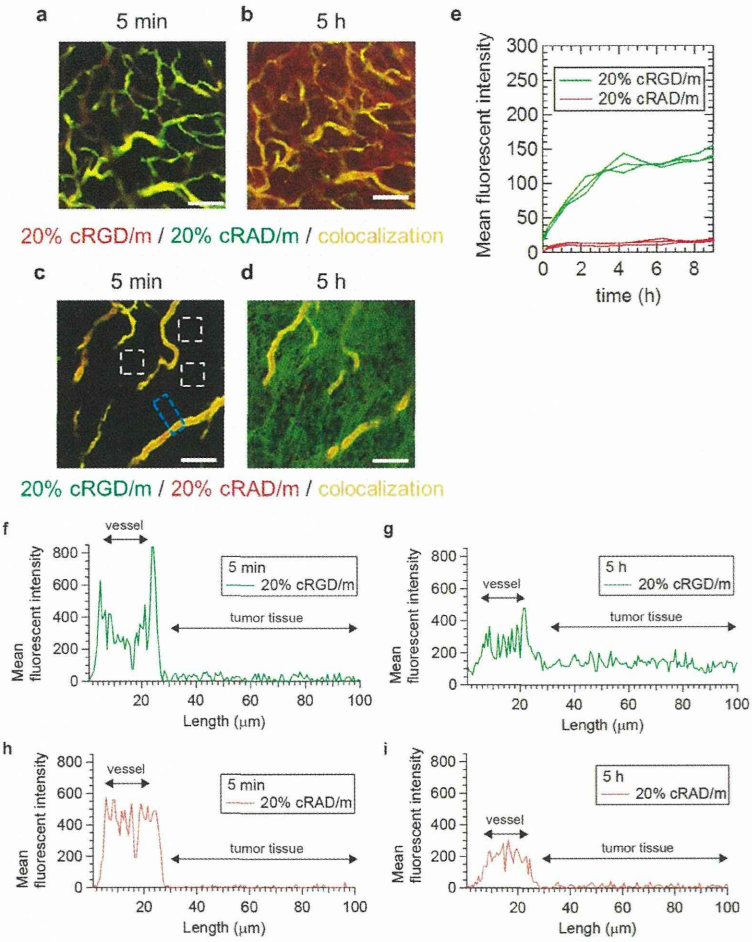

Figure 6. IVCLSM of DACHPt/m. IVCLSM observations of 20% cRAD/m (green) and 20% cRGD/m (red) in blood vessels and tumors at (a) 5 min and (b) 5 h after intravenous coadministration. IVCLSM observations of 20% cRAD/m (red) and 20% cRGD/m (green) in blood vessels and tumors at (c) 5 min and (d) 5 h after intravenous coadministration. Their colocalization is shown in yellow. The spectral images were unmixed to determine the Alexa 647 (red), Dylight 488 (green), and autofluorescence levels. Scale bars represent 100 μm in all images. (e) Quantitative analysis of the amounts of micelles in tumor sites based on the IVCLSM results. Fluorescence profiles of cRGD/m (green) and cRAD/m (red) in the region selected (indicated by a white rectangle in part c). (d) Permeation profiles of 20% cRGD/m (green) and 20% cRAD/m (red) from the blood vessels to the tumors in the selected region (indicated by a blue rectangle in part c) at 5 min (f and h) and at 5 h (g and i).

fluorescence signal of cRGD/m along the lining of the tumor vessel was confirmed 5 min after administration. Then, the intensity values of green fluorescence (cRGD/m) at the tumor tissue increased from 0 to approximately 150 during the initial 5 h (Figure 6g). On the other hand, the cRAD/m (red) was unable to penetrate tumor vasculature (Figure 6h and i). We confirmed that subcutaneous glioblastoma models showed the expression of "tight junctions" (Claudin 5-positive) and "pericytes" (αSMA-positive) (Supporting Information Figure S3) by immunohistochemical analysis,[46−48] indicating the existence of the vascular/tumor barriers. Hence, we proved that this differential permeability is attributed to the potential of cRGD ligands on the micelles to induce integrin-mediated active transport specifically through the vascular barrier. Overall, it is reasonable to conclude that the cRGD/m can enter the tumor sites *via* active transport-mediated pathways, most likely transcytosis as the vesicular transport is enhanced in the vasculature of brain tumor.[49,50] Although the integrin targeting by using cRGD has been considerably investigated, the direct visual evidence to support active transport across the vascular barrier of glioblastoma is reported for the first time in this study as far as we know.

Further research into the antitumor efficacy by utilizing orthotopic brain tumor models would clarify the availability of cRGD/m in clinical settings. We implanted U87MG-Luc2 cancer cells into the brains of BALB/c nude mice (Supporting Information) and monitored the tumor growth inhibition effect by luciferase imaging. Five days after tumor inoculation, 20% cRGD/m and 20% cRAD/m were administered iv at a dose of 4 mg/kg on a DACHPt basis every other day (total of three injections). Oxaliplatin (dose = 8 mg/kg) was also used as a control-free drug with the same dosing schedule. The IVIS images showed that the signals from

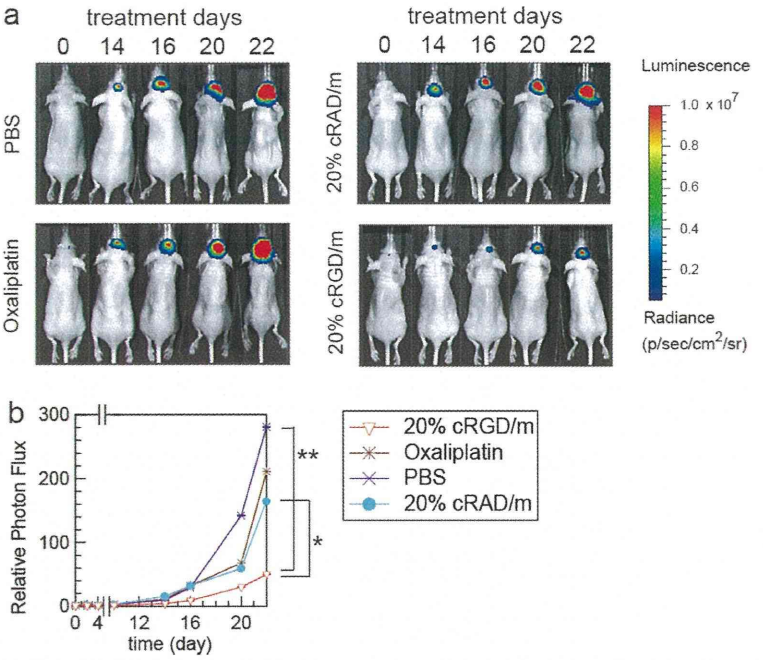

Figure 7. Effects of cRGD-linked DACHPt/m in orthotopic U87MG glioblastoma. The mice were anesthetized with isoflurane and injected intravenously with 150 mg/kg luciferin. At 1−2 min after luciferin injection, the mice were imaged for 1−60 s. (a) Representative *in vivo* bioluminescence images of the mice from PBS-, oxaliplatin-, 20% cRAD/m-, and 20% cRGD/m-treated groups. The colored scale bar indicates the intensity of bioluminescence in p/s/cm^2/sr. (b) Comparison of tumor growth inhibition with 20% cRGD/m and 20% cRAD/m. Five days after tumor cell transplantation, the mice were injected intravenously with micelles. The micelles (4 mg/kg based on DACHPt) were administered every other day (three injections). Oxaliplatin was used as a control platinum drug (dose = 8 mg/kg) with the same treatment schedule. Data represent mean ± SEM (n = 12). Two-way ANOVA was used to analyze differences in the tumor mass volume, and $^{**}p < 0.001$ and $^{*}p < 0.01$ were considered significant.

the cRGD/m-administrated group were clearly weaker than other groups (Figure 7a). On the basis of the quantification of the bioluminescent data from the head area on day 22, approximately 5-fold lower photon flux was observed in the mice treated with 20% cRGD/m compared to those treated with oxaliplatin and 20% cRAD/m (Figure 7b). These results indicate that cRGD is a key to deliver the PM into orthotopic brain tumor models. Altogether, we found that linkage of the ligand molecule cRGD to PMs allows active transport-mediated penetration into tumor tissue beyond BBTB in brain tumor models, achieving potent antitumor activity.

CONCLUSION

In this study, we designed and synthesized a series of DACHPt/m with different percentages of cRGD ligand for the treatment of brain tumors. The constructs and their properties were fully characterized and subjected to *in vitro* and *in vivo* studies, including cytotoxicity assays, cellular uptake analyses, and evaluations of therapeutic efficacy in tumor-bearing mice. Consequently, 20% cRGD/m exhibited significantly higher growth inhibitory effect against GBM tumors compared to the nontargetable 20% cRAD/m. Furthermore, the IVCLSM results demonstrated the tumor-accumulation characteristics of cRGD/m, which prompted the identification of the active transport of cRGD-mediated drug delivery across vascular and tumor barriers, *i.e.*, BBTB. These findings indicate that cRGD-mediated DDS is a powerful strategy for targeting therapy of glioblastoma through the facilitated drug delivery beyond the BBTB.

MATERIALS AND METHODS

Materials, Cell Lines, and Animals. Information regarding materials, cell line (human glioblastoma cell line (U87MG)), and animals (BALB/c nude mice; Oriental Yeast Co., Ltd., Tokyo, Japan) is described in the Supporting Information. All animal experiments were performed in accordance with the Guidelines for the Care and Use of Laboratory Animals as stated by the University of Tokyo.

Preparation of Polymers and PMs. Poly(ethylene glycol)-*b*-poly(L-glutamic acid) (MeO-PEG-*b*-P(Glu)) and maleimide-conjugated poly(ethylene glycol)-*b*-poly(L-glutamic acid) (Mal-PEG-*b*-P(Glu)) were designed and synthesized based on our developed methods.[35,39,40] MeO-PEG-*b*-P(Glu) was fluorescently labeled by conjugating the Dylight 488, Alexa 555, and Alexa 647 succinimidyl esters to the ω-amino groups of polymers. The polymers were characterized by ^{1}H NMR measurement (solvent: $CDCl_3$, D_2O, and *d*-DMSO; temperature: 25 °C), size exclusion chromatography in DMF containing lithium bromide (10 mM) or in 10 mM PBS containing 150 mM NaCl, and high-performance liquid chromatography in 2 mM PB (pH = 6.5). Details of the procedures used for

polymer synthesis and characterization are described in the Supporting Information. DACHPt/m, cRGD/m, and cRAD/m were prepared according to a method described previously, with a slight modification. In brief, the typical procedure used for the preparation of 20% cRGD/m was as follows: a mixture of DACHPt-(NO_3)Cl, MeO-PEG-*b*-P(Glu), and Mal-PEG-*b*-P(Glu) ([Glu] = 5 mmol/L, [DACHPt]/[Glu] = 1.0 (mol/mol), and [MeO-PEG-*b*-P(Glu)]/[Mal-PEG-*b*-P(Glu)] = 1.0/1.0 (mol/mol)) was stirred at 37 °C for 120 h. The reaction mixture was transferred to a cellophane tube (Spectra/Pro 6 membrane: MWCO, 3500) and dialyzed for 1 day against distilled water, followed by ultrafiltration (MWCO, 30 000) to yield the maleimide-functionalized DACHPt/m. Next, cyclo[RGDfK(CX-)] (cRGD peptide, X = ε-Acp) was added to the maleimide-functionalized DACHP/m solution and incubated at rt. After 18 h, the micelle solution was purified by ultrafiltration (MWCO, 100 000) to give the 20% cRGD-linked DACHPt/m (20% cRGD/m). The number of cRGD linked was estimated by ^{1}H NMR measurement (solvent, D_2O; temperature, 25 °C). The control DACHPt/m (ctrl/m), 5% and 40% cRGD-linked (5% cRGD/m and 40% cRGD/m), and 20% cRAD-linked (20% cRAD/m) DACHPt/m were prepared in the same manner as described above, with the slight exception that the molar ratios of [MeO-PEG-*b*-P(Glu)/Mal-PEG-*b*-P(Glu)] were changed from 50/50 to 100/0 for ctrl/m, 10/90 for 5% cRGD/m, and 0/100 for 40% cRGD/m. The size distribution of DACHPt/m was evaluated by DLS measurements at 25 °C, and the zeta potentials of the micelles were measured in phosphate buffer at pH 7.4 using a Zetasizer Nano ZS90 (Malvern Instruments). The platinum content of the micelles was determined by ICP-MS using a Hewlett-Packard HP 4500 ICP-MS system. More detailed information is provided in the Supporting Information.

Cellular Uptake of the Platinum Drug. U87MG cells (2×10^7) were seeded into a 225 cm^2 cell culture flask. After 12 h incubation, the medium was replaced with fresh medium (30 mL), which included 10 μM (on a platinum basis) oxaliplatin or micelles. Then, cells were incubated for 1, 3, 8, and 24 h. The cells were then washed three times with PBS, scraped, and harvested. The cells were resuspended in 1000 μL of water and freeze-dried to yield the dried samples. Acid digestion of all samples was carried out with *ca.* 1.0 mL of concentrated HNO_3 at 200 °C, and then the dried samples were dissolved in 1 vol % HNO_3(aq) (1.0 mL). Platinum concentration was measured by ICP-MS. All experiments were repeated four times, and the average platinum content (μg)/2×10^7 cells was calculated.

***In Vitro* Cytotoxicity Assay.** The 50% growth inhibitory concentrations (IC_{50}) of free oxaliplatin, ctrl/m, the 5%, 20%, and 40% cRGD/m, and 20% cRAD/m were evaluated in U87MG cells using the Cell Counting Kit-8 (Dojindo Laboratories). The cells (2000 cells/50 μL) were cultured in DMEM containing 10% FBS in a 96-well multiplate. The cells were then exposed to oxaliplatin or the micelles for 48 h. The manufacturer's reagent (10 μL) was added, and then the cells were incubated for 2 h. The absorbance of media was measured at 450 nm using a microplate reader (Biorad). The inhibitory effect after short-term drug exposure was tested in the same manner as described above, with the following slight difference: different concentrations of oxaliplatin solution or micelle solution were added to the 96-well multiplate, and the cells were incubated for 3 h. The medium was replaced with fresh medium (100 μL) and incubated for 48 h. The experiments were repeated three times, and the average IC_{50} values were calculated.

Antitumor Activity Assay. In order to evaluate the antitumor efficacy of DACHPt/m using different molarities of ligand molecules, subcutaneous tumor models in BALB/c nude mice (Oriental Yeast Co., Ltd., Tokyo, Japan) (n = 6) were treated three times intravenously every other day with 4 mg/kg (on a DACHPt basis) of 20% cRGD/m and 20% cRAD/m. The antitumor activities were evaluated by measuring the tumor size (V), which was estimated using the following equation: $V = ab^2/2$, where a and b are the major and minor axes of the tumor measured using a Vernier microcaliper. In the antitumor activity assay using orthotopic tumor models, BALB/c nude mice (n = 12) were treated three times intravenously every other days with 4 mg/kg (on a DACHPt basis) of 20% cRGD/m and 20% cRAD/m. *In vivo* imaging was performed using an IVIS Spectrum (Xenogen Corporation). Luciferin (Promega) was used as a substrate for luciferase. The mice were anesthetized with isoflurane (Mylan Inc.) and injected intravenously with 150 mg/kg luciferin. At 1−2 min after luciferin injection, the mice were imaged for 1−60 s. The regions of interest (ROIs) were selected to measure the tumor volume and background. The photons emitted from ROIs were quantified using Living Image software (ver. 4.1). *In vivo* luciferase activity was expressed as photons/s/cm^2/sr. Two-way analysis of variance (ANOVA) was used to analyze the differences in the tumor mass volume between the experimental and control groups. Data analysis was performed using GraphPad Prism version 5.04 for Windows (GraphPad Software). $^{**}p < 0.001$ was considered statistically significant in each analysis.

Plasma Clearance and Tumor Accumulation of DACHPt/m. To evaluate the plasma clearance and tumor accumulation of DACHPt/m *in vivo*, BALB/c nude mice bearing U87MG tumors (n = 6) were intravenously injected with 20% cRGD/m, 20% cRAD/m, and oxaliplatin at 100 mg/mouse on a DACHPt basis. The mice were sacrificed 1, 4, 8, and 24 h after injection. The tumors were excised, washed with PBS, and weighed after removing excess fluid. Blood was collected from the inferior vena cava, heparinized, and centrifuged to obtain the plasma. Acid digestion of all samples was carried out using *ca.* 1.0 mL of concentrated HNO_3 at 200 °C, and the dried samples were dissolved in 1 vol % HNO_3(aq) (1.0 mL). Platinum concentration was measured by ICP-MS.

IVCLSM. IVCLSM was performed using a Nikon A1R confocal laser scanning microscope system attached to an upright ECLIPSE FN1 machine, which was equipped with a Plan Apo VC 20× DIC N2 (numerical aperture: 0.75) objective lens (Nikon), as described in our previous report.[37] All pictures/movies were acquired as spectral images using 10 μm of confocal slices. Video images of the tumors were aquired at 5 min intervals for 15 min. Video acquisition was continued at 1 h intervals. Two-hundred microliters of solution containing Dylight 488- and Alexa 647-labeled micelles was administered *via* a tail vein catheter. The AFU value of each micelle solution was adjusted to *ca.* 6000 measured by NanoDrop. Video acquisition was initiated 280 s after administration. Dylight 488 and Alexa 647 were excited using lasers at wavelengths of 488 and 638 nm, respectively. Acquired data were processed using Nikon NIS Elements (ver. 4.00.06). The spectral images were unmixed with respect to Dylight 488, Alexa 647, and autofluorescence. ROIs were selected manually using Nikon NIS Elements (ver. 4.00.06).

Conflict of Interest: The authors declare no competing financial interest.

Acknowledgment. We thank C. Sakamoto, R. Shiratori, and N. Henzan for the synthesis of polymers, and S. Ogura and A. Miyoshi for help with animal experiments. This work was supported by the Funding Program for World-Leading Innovative R&D on Science and Technology (FIRST Program) from the Japan Society for the Promotion of Science (JSPS) and Grants-in-Aid for Scientific Research from the Japanese Ministry of Health, Labour and Welfare (MHLW). It was partially supported by Grants-in-Aid for Young Scientists (A), Challenging Exploratory Research, and JSPS Fellows.

Supporting Information Available: Details of the materials, measurement techniques, synthesis of polymers, micelle preparation, information on the biological experiments related to the knockdown of intregrin alpha V, real-time PCR, detection of integrin receptors, and animal preparation, and IVCLSM video. This material is available free of charge *via* the Internet at http://pubs.acs.org.

REFERENCES AND NOTES

1. Rat, J. S. Molecular Mechanisms of Glioma Invasiveness: The Role of Proteases. *Nat. Rev. Cancer* **2003**, *3*, 489–501.
2. Arko, L.; Katsyv, I.; Park, G. E.; Luan, W. P.; Park, J. K. Experimental Approaches for the Treatment of Malignant Gliomas. *Pharmacol. Ther.* **2010**, *128*, 1–36.
3. Mangiola, A.; Anile, C.; Pompucci, A.; Capone, G.; Rigante, L.; De Bonis, P. Glioblastoma Therapy: Going Beyond Hercules Columns. *Expert Rev. Neurother.* **2010**, *10*, 507–514.

4. Jain, R. K.; Tomaso, di E.; Duda, D. G.; Loeffler, J. S.; Sorensen, A. G.; Batchelor, T. T. Angiogenesis in Brain Tumours. *Nat. Rev. Neurosci.* **2008**, *8*, 610–622.
5. Wen, P. Y.; Kesari, S. Malignant Gliomas in Adults. *N. Engl. J. Med.* **2008**, *359*, 492–507.
6. Avgeropoulos, N. G.; Batchelor, T. T. New Treatment Strategies for Malignant Gliomas. *Oncologist* **1999**, *4*, 209–224.
7. Jones, T. S.; Holland, E. C. Standard of Care Therapy for Malignant Glioma and Its Effect on Tumor and Stromal Cells. *Oncogene* **2012**, *31*, 1995–2006.
8. Rich, J. N.; Bigner, D. D. Development of Novel Targeted Therapies in the Treatment of Malignant Glioma. *Nat. Rev. Drug Discovery* **2004**, *3*, 430–446.
9. Reardon, D. A.; Perry, J. R.; Brandes, A. A.; Jalali, R.; Wick, W. Advances in Malignant Glioma Drug Discovery. *Expert Opin. Drug Discovery* **2011**, *6*, 739–753.
10. Groothuis, D. R. The Blood-Brain and Blood-Tumor Barriers: A Review of Strategies for Increasing Drug Delivery. *Neuro-Oncology* **2000**, *2*, 45–59.
11. Ningaraj, N. S. Drug Delivery to Brain Tumours: Challenges and Progress. *Expert Opin. Drug Delivery* **2006**, *3*, 499–509.
12. Sarin, H. Recent Progress towards Development of Effective Systemic Chemotherapy for the Treatment of Malignant Brain Tumors. *J. Transl. Med.* **2009**, *7*, 77.
13. He, H.; Li, Y.; Jia, X. R.; Du, J.; Ying, X.; Lu, W. L.; Lou, J. N.; Wei, Y. PEGylated Poly(amidoamine) Dendrimer-Based Dual-Targeting Carrier for Treating Brain Tumors. *Biomaterials* **2011**, *32*, 478–487.
14. Xin, H.; Jiang, X.; Gu, J.; Sha, X.; Chen, L.; Law, K.; Chen, Y.; Wang, X.; Jiang, Y.; Fang, X. Angiopep-Conjugated Poly(ethylene glycol)-co-Poly(ε-caprolactone) Nanoparticles as Dual-Targeting Drug Delivery System for Brain Glioma. *Biomaterials* **2011**, *32*, 4293–4305.
15. Pardridge, W. M. Drug and Gene Delivery to the Brain: The Vascular Route. *Neuron* **2002**, *36*, 555–558.
16. Muldoon, L. L.; Soussain, C.; Jahnke, K.; Johanson, C.; Siegal, T.; Smith, Q. R.; Hall, W. A.; Hynynen, K.; Senter, P. D.; Peereboom, D. M.; *et al.* Chemotherapy Delivery Issues in Central Nervous System Malignancy: A Reality Check. *J. Clin. Oncol.* **2007**, *25*, 2295–2305.
17. Liu, Y.; Lu, W. Recent Advances in Brain Tumor-Targeted Nano-Drug Delivery Systems. *Expert Opin. Drug Delivery* **2012**, *9*, 671–686.
18. Chen, C.; Xu, T.; Lu, Y.; Chen, J.; Wu, S. The Efficacy of Temozolomide for Recurrent Glioblastoma Multiforme. *Eur. J. Neurol.* **2013**, *20*, 223–230.
19. Duncan, R. The Dawning Era of Polymer Therapeutics. *Nat. Rev. Drug Discovery* **2003**, *2*, 347–360.
20. Ferrari, M. Cancer Nanotechnology: Opportunities and Challenges. *Nat. Rev. Cancer* **2005**, *5*, 161–171.
21. Torchilin, V. P. Recent Advances with Liposomes as Pharmaceutical Carriers. *Nat. Rev. Drug Discovery* **2005**, *4*, 145–160.
22. Davis, M. E.; Chen, Z.; Shin, D. Nanoparticle Therapeutics: An Emerging Treatment Modality for Cancer. *Nat. Rev. Drug Discovery* **2008**, *7*, 771–782.
23. Kataoka, K.; Harada, A.; Nagasaki, Y. Block Copolymer Micelles for Drug Delivery: Design, Characterization and Biological Significance. *Adv. Drug Delivery Rev.* **2001**, *47*, 113–131.
24. Nishiyama, N.; Kataoka, K. Current State, Achievements, and Future Prospects of Polymeric Micelles as Nanocarriers for Drug and Gene Delivery. *Pharmacol. Ther.* **2006**, *112*, 630–648.
25. Danhier, F.; Breton, A. L.; Préat, V. RGD-Based Strategies to Target Alpha(v) Beta(3) Integrin in Cancer Therapy and Diagnosis. *Mol. Pharmaceutics* **2012**, *9*, 2961–2973.
26. Matsumura, Y.; Maeda, H. A New Concept for Macromolecular Therapeutics in Cancer Chemotherapy: Mechanism of Tumouritropic Accumulation of Proteins and the Antitumour Agent SMANCS. *Cancer Res.* **1986**, *46*, 6387–6392.
27. Hobbs, S. K.; Monsky, W. L.; Yuan, F.; Roberts, W. G.; Griffith, L.; Torchilin, V. P.; Jain, R. K. Regulation of Transport Pathways in Tumor Vessels: Role of Tumor Type and Microenvironment. *Proc. Natl. Acad. Sci. U.S.A.* **1998**, *95*, 4607–4612.
28. Hynes, R. O. A Reevaluation of Integrins as Regulators of Angiogenesis. *Nat. Med.* **2001**, *8*, 918–912.
29. Hood, J. D.; Cheresh, D. A. Role of Integrins in Cell Invasion and Migration. *Nat. Rev. Cancer* **2002**, *2*, 91–100.
30. Desgrosellier, J. S.; Cheresh, D. A. Integrins in Cancer: Biological Implications and Therapeutic Opportunities. *Nat. Rev. Cancer* **2010**, *10*, 9–22.
31. Taga, T.; Suzuki, A.; Gonzalez-Gomez, I.; Gilles, F. H.; Stins, M.; Shimada, H.; Barsky, L.; Weinberg, K. I.; Laug, W. E. αv-Integrin Antagonist EMD 121974 Induces Apoptosis in Brain Tumor Cells Growing on Vitronectin and Tenascin. *Int. J. Cancer* **2002**, *98*, 690–697.
32. Sheldrake, H. M.; Patterson, L. H. Function and Antagonism of Beta3 Integrins in the Development of Cancer Therapy. *Curr. Cancer Drug Targets* **2009**, *9*, 519–540.
33. Zhan, C.; Gu, B.; Xie, C.; Li, J.; Liu, Y.; Lu, W. Cyclic RGD Conjugated Poly(ethylene glycol)-co-Poly(lactic acid) Micelle Enhances Paclitaxel Anti-Glioblastoma Effect. *J. Controlled Release* **2010**, *143*, 136–142.
34. Zhan, C.; Wei, X.; Qian, J.; Feng, L.; Zhu, J.; Lu, W. Co-Delivery of TRAIL Gene Enhances the Anti-Glioblastoma Effect of Paclitaxel *in Vitro* and *in Vivo*. *J. Controlled Release* **2012**, *160*, 630–636.
35. Cabral, H.; Matsumoto, Y.; Mizuno, K.; Chen, Q.; Murakami, M.; Kimura, M.; Terada, Y.; Kano, M. R.; Miyazono, K.; Uesaka, M.; *et al.* Accumulation of Sub-100 nm Polymeric Micelles in Poorly Permeable Tumours Depends on Size. *Nat. Nanotechnol.* **2011**, *6*, 815–823.
36. Murakami, M.; Cabral, H.; Matsumoto, Y.; Wu, S.; Kano, M. R.; Yamori, T.; Nishiyama, N.; Kataoka, K. Improving Drug Potency and Efficacy by Nanocarrier-Mediated Subcellular Targeting. *Sci. Transl. Med.* **2011**, *3*, 64ra2.
37. Matsumoto, Y.; Nomoto, T.; Cabral, H.; Matsumoto, Y.; Watanabe, S.; Christie, R. J.; Miyata, K.; Oba, M.; Ogura, T.; Yamasaki, Y.; *et al.* Direct and Instantaneous Observation of Intravenously Injected Substances using Intravital Confocal Micro-Videography. *Biomed. Opt. Express* **2010**, *1*, 1209–1216.
38. Nomoto, T.; Matsumoto, Y.; Miyata, K.; Oba, M.; Fukushima, S.; Nishiyama, N.; Yamasoba, T.; Kataoka, K. *In Situ* Quantitative Monitoring of Polyplexes and Polyplex Micelles in the Blood Circulation Using Intravital Real-Time Confocal Laser Scanning Microscopy. *J. Controlled Release* **2011**, *151*, 104–109.
39. Cabral, H.; Nishiyama, N.; Okazaki, S.; Kato, Y.; Kataoka, K. Preparation and Biological Properties of Dichloro(1,2-diaminocyclohexane)platinum(II) (DACHPt)-Loaded Polymeric Micelles. *J. Controlled Release* **2005**, *101*, 223–232.
40. Cabral, H.; Nishiyama, N.; Kataoka, K. Optimization of (1,2-Diaminocyclohexane)platinum(II)-Loaded Polymeric Micelles Directed to Improved Tumour Targeting and Enhanced Antitumour Activity. *J. Controlled Release* **2007**, *121*, 146–155.
41. Yamada, S.; Bu, X. Y.; Khankaldyyan, V.; Gonzales-Gomez, I.; McComb, J. G.; Laug, W. E. Effect of the Angiogenesis Inhibitor Cilengitide (EMD 121974) on Glioblastoma Growth in Nude Mice. *Neurosurgery* **2006**, *59*, 1304–1312.
42. Carter, A. Integrins as Target: First Phase III Trial Launches, But Questions Remain. *J. Natl. Cancer Inst.* **2010**, *102*, 675–677.
43. Fink, K.; Mikkelsen, T.; Nabors, L. B.; Ravin, P.; Plotkin, S. R.; Schiff, D.; Hicking, C.; Picard, M.; Reardon, D. A. Long-Term Effects of Cilengitide, a Novel Integrin Inhibitor, in Recurrent Glioblastoma: A Randomized Phase IIa Study. *J. Clin. Oncol.* **2010**, *28*, 182s.
44. Mikkelsen, T.; Brodie, C.; Finniss, S.; Berens, M. E.; Rennert, J. L.; Nelson, K.; Lemke, N.; Brown, S. L.; Hahn, D.; Neuteboom, B.; *et al.* Radiation Sensitization of Glioblastoma by Cilengitide Has Unanticipated Schedule-Dependency. *Int. J. Cancer* **2009**, *124*, 2719–2727.
45. Nabors, L. B.; Mikkelsen, T.; Rosenfeld, S. S.; Hochberg, F.; Akella, N. S.; Fisher, J. D.; Cloud, G. A.; Zhang, Y.; Carson, K.; Wittemer, S. M.; *et al.* Phase I and Correlative Biology Study of Cilengitide in Patients with Recurrent Malignant Glioma. *J. Clin. Oncol.* **2007**, *25*, 1651–1657.

46. Morita, K.; Sasaki, H.; Furuse, K.; Furuse, M.; Tsukita, S.; Miyachi, Y. Expression of Claudin-5 in Dermal Vascular Endothelia. *Exp. Dermatol.* **2003**, *12*, 289–295.
47. Cooper, I.; Cohen-Kashi-Malina, K.; Teichberq, V. I. Claudin-5 Expression in *in Vitro* Models of the Blood-Brain Barrier. *Methods Mol. Biol.* **2011**, *762*, 347–354.
48. Jiao, H.; Wang, Z.; Liu, Y.; Wang, P.; Xue, Y. Specific Role of Tight Junction Proteins Claudin-5, Occludin, and ZO-1 of the Blood-Brain Barrier in a Focal Cerebral Ischemic Insult. *J. Mol. Neurosci.* **2011**, *44*, 130–139.
49. Stewart, P. A.; Hayakawa, K.; Farrell, C. L.; Del Maestro, R. F. Quantitative Study of Microvessel Ultrastructure in Human Peritumoral Brain Tissue. Evidence for a Blood-Brain Barrier Defect. *J. Neurosurg.* **1987**, *67*, 697–705.
50. Stewart, P. A. Endothelial Vesicles in the Blood-Brain Barrier: Are They Related to Permeability? *Cell. Mol. Neurobiol.* **2000**, *20*, 149–163.

JACS
JOURNAL OF THE AMERICAN CHEMICAL SOCIETY

Article

pubs.acs.org/JACS

Phenylboronic Acid-Installed Polymeric Micelles for Targeting Sialylated Epitopes in Solid Tumors

Stephanie Deshayes,[†,◆] Horacio Cabral,[‡,◆] Takehiko Ishii,[‡] Yutaka Miura,[§,∥] Shutaro Kobayashi,[†] Takashi Yamashita,[⊥] Akira Matsumoto,[#] Yuji Miyahara,[#] Nobuhiro Nishiyama,[○] and Kazunori Kataoka*[,†,‡,∥,▽]

[†]Department of Materials Engineering, [‡]Department of Bioengineering, [§]Division of Tissue Engineering, and [∥]Center for Disease Biology and Integrative Medicine, Graduate School of Engineering, The University of Tokyo, 7-3-1 Hongo, Bunkyo-ku, Tokyo 113-8656, Japan

[⊥]Department of Pure and Applied Chemistry, Graduate School of Science and Technology, Tokyo University of Science, 2641 Yamazaki, Noda-shi, Chiba-ken 278-8510, Japan

[#]Institute of Biomaterials and Bioengineering, Tokyo Medical and Dental University, 2-3-10 Kanda-Surugadai, TokyoChiyoda-ku, 101-0062, Japan

[○]Polymer Chemistry Division, Chemical Resources Laboratory, Tokyo Institute of Technology, R1-11, 4259 Nagatsuta, Midori-ku, Yokohama 226-8503, Japan

[▽]Center for NanoBio Integration, The University of Tokyo, 7-3-1 Hongo, Bunkyo-ku, Tokyo 113-8656, Japan

Supporting Information

ABSTRACT: Ligand-mediated targeting of nanocarriers to tumors is an attractive strategy for increasing the efficiency of chemotherapies. Sialylated glycans represent a propitious target as they are broadly overexpressed in tumor cells. Because phenylboronic acid (PBA) can selectively recognize sialic acid (SA), herein, we developed PBA-installed micellar nanocarriers incorporating the parent complex of the anticancer drug oxaliplatin, for targeting sialylated epitopes overexpressed on cancer cells. Following PBA-installation, the micelles showed high affinity for SA, as confirmed by fluorescence spectroscopy even at intratumoral pH conditions, i.e., pH 6.5, improving their cellular recognition and uptake and enhancing their *in vitro* cytotoxicity against B16F10 murine melanoma cells. *In vivo*, PBA-installed micelles effectively reduced the growth rate of both orthotopic and lung metastasis models of melanoma, suggesting the potential of PBA-installed nanocarriers for enhanced tumor targeting

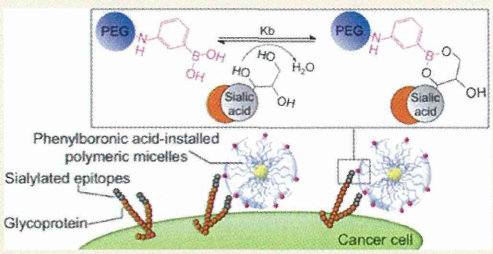

INTRODUCTION

Nanocarriers have shown great potential for selectively delivering high payloads of therapeutic molecules to tumors.[1−5] When systemically injected, long-circulating nanocarriers can specifically accumulate in solid tumors due to the increased permeability of the tumor vasculature and be retained because of the impaired lymphatic drainage at the cancerous site.[6] By functionalization of the surface of these nanocarriers with ligands capable of recognition of cell-specific surface receptors, they can be rendered with cellular selectivity and superior intracellular delivery.[2,3,7−12] Thus, antibodies,[8] antibody fragments,[9] aptamers,[10] peptides,[11,12] and small molecules[13] have been used as ligands for improving the tumor targeting ability of nanocarriers. The efficiency of ligand-installed nanocarriers for targeting cancer cells is affected by several features, such as the binding affinity of the ligands to the receptors, the rate of internalization, the density and availability of the receptors, the intratumoral distribution of the receptors and the variation of the receptor expression with the tumor stage.[7−13] Therefore, effective approaches for ligand-mediated targeting of nanocarriers require suitable recognition of the versatile receptor landscapes of tumors.

Carbohydrate antigens, which are expressed in all tumor cells due to aberrant glycosylation[14−16] represent an exceptional target for ligand-mediated targeting of nanocarriers, as they are displayed in tumors more frequently than oncogene markers, such as HER2/neu.[15] These malignant glycophenotypes overexpress sialylated epitopes, i.e., glycan chains containing *N*-acetylneuraminic acid (Neu5Ac), which is the predominant sialic acid (SA) in humans.[14−16] The increased expression of sialylated antigens on cancer cells is closely related with cancer progression and with poor prognosis in patients with lung, breast, colon, prostate, bladder, and stomach cancer.[14−16] Moreover, hypoxic regions of solid tumors have shown increased levels of sialylated antigens,[17] and the overexpression of sialylated glycans, such as Sialyl-Lewis^x and Sialyl-Lewis^a, is important for the formation of metastases.[18] SA has been

Received: June 24, 2013
Published: September 12, 2013

   dx.doi.org/10.1021/ja406406h | J. Am. Chem. Soc. 2013, 135, 15501−15507

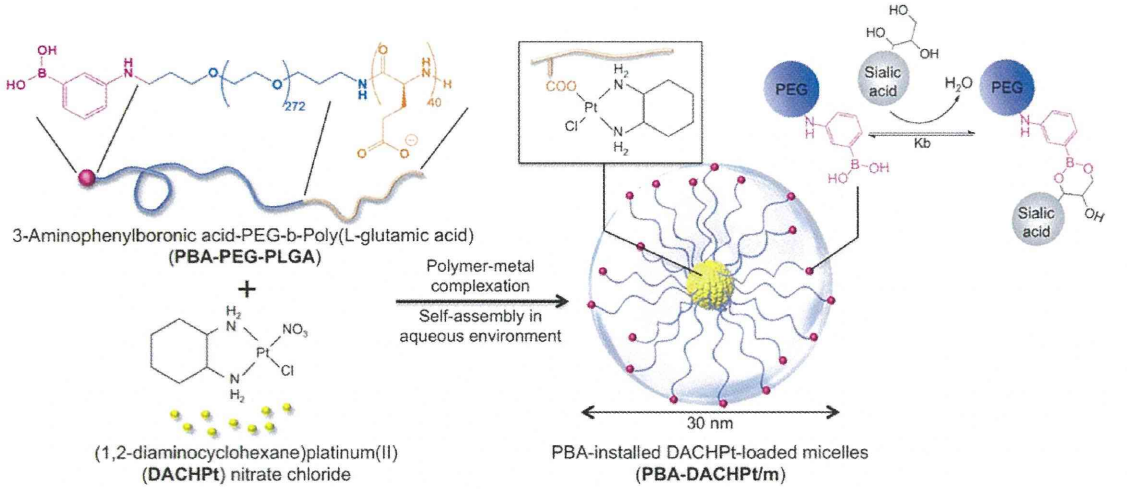

Figure 1. Preparation of PBA-installed DACHPt-loaded micelles by self-assembly through polymer–metal complex formation between DACHPt and PBA-poly(ethylene glycol)-*b*-poly(L-glutamic acid) in distilled water. PBA moieties on the surface of the micelles can bind to SA.

targeted *in vitro* by using lectin[19] and antibodies,[20] such as the tumoral marker CA19-9, used for detection of Sialyl-Lewis[a] in gastrointestinal tumors. Nevertheless, these approaches have been difficult to translate *in vivo*, mainly because of their immunogenicity. Moreover, as SA is also present on red blood cells and the luminal surfaces of vascular endothelium,[21,22] systemically injected ligands for SA targeting should not be active until reaching the site of tumors.

We have recently demonstrated the ability of phenylboronic acid (PBA) for selective recognition of SA overexpressed on the surface of cancer cells.[23] Although PBA can also form complexes with other common sugars, they are unstable unless formed at pHs higher than its pK_a value, whereas the complex between PBA and SA is stable even at pHs lower than its pK_a.[24,25] This feature, with controlled pK_a of PBA, provides a molecular basis for the specific SA recognition at physiological pH. This interaction has been recently used for determining the sialylation status of solid tumors by MRI through PBA-based reporters.[26] In addition to the high affinity and selectivity for SA, PBA presents several advantages for targeting of cancer cells such as being nontoxic, nonimmunogenic, and inexpensive.

Herein, we developed PBA-functionalized nanocarriers by installing PBA moieties on the polymeric micelles for specific targeting of SA epitopes overexpressed on tumor cells. Polymeric micelles, i.e., core–shell self-assemblies of block copolymers, provide multiple advantages as nanocarriers including their nanoscaled size, their poly(ethylene glycol) (PEG) shell, which prevents their recognition by macrophages of the reticuloendothelial system (RES) and prolongs their blood circulation time, and hydrophobic core for loading and controlled release of bioactive molecules.[4,5,27−29] Our polymeric micelles incorporating the anticancer drugs paclitaxel, SN-38, cisplatin, and the parent complex of oxaliplatin, i.e., dichloro(1,2-diamino-cyclohexane)platinum(II) (DACHPt), have advanced to clinical studies,[30,31] demonstrating high efficacy against several intractable tumors, such as triple-negative breast cancers, and less side effects in patients.[30] In this study, we use DACHPt-loaded micelles (DACHPt/m), which have shown selective accumulation in tumor tissues and strong suppression of the growth of several tumor models,[32−35] to prepare polymeric micelles having PBA moieties on their surface. The micelles were self-assembled through the coordination bond between platinum drug and the carboxylic groups of PBA-poly(ethylene glycol)-*b*-poly(L-glutamic acid) [PBA-PEG-*b*-PLGA] copolymers in water (Figure 1). The inherent fluorescence of PBA installed to PEG-*b*-PLGA copolymers was used for studying its binding affinity against different sugars by fluorescence spectroscopy. Moreover, the ability of PBA-installed DACHPt/m (PBA-DACHPt/m) to target SA in tumors was evaluated *in vitro* as well as *in vivo* against orthotopic and metastatic tumor models. For this purpose, highly metastatic B16F10 murine melanoma cells overexpressing SA on their surface[36] were used, for which we have recently established a method of quantification based on the PBA-SA interaction.[23] Our results showed a high selectivity of PBA-DACHPt/m to SA epitopes, which enhanced their cellular uptake *in vitro* and improved their tumor accumulation and retention *in vivo*, leading to a superior antitumor effect.

■ RESULTS AND DISCUSSION

Preparation of PBA End-Functionalized PEG-*b*-PLGA. Acetal-poly(ethylene glycol)-*b*-poly(L-glutamic acid) [acetal-PEG-*b*-PLGA] block copolymer was reacted with 3-aminophenylboronic acid by one pot reductive amination to afford aminophenylboronic acid-poly(ethylene glycol)-*b*-poly(L-glutamic acid) [PBA-PEG-*b*-PLGA] copolymer (Scheme S1). Thus, after deprotection of the acetal residue under acidic conditions, the obtained aldehyde group formed a Schiff base with 3-amino-substituted PBA. This intermediate imine was reduced to a secondary amine by using $NaBH_3CN$. The PBA installation at PEG end was confirmed to be almost quantitative by the proton ratios of the aromatic group of PBA and the ethylene units in PEG in the ^1H NMR spectrum (Figure S1).

Binding Affinities of PBA-PEG-*b*-PLGA to Various Sugars. Most sugars can complex only with the tetrahedral anionic form of boronate, because the complex with the trigonal neutral form is usually susceptible to hydrolysis.[37] In contrast, SA-PBA complexation is also favored by the trigonal form, for which involvement of multiple metastable binding sites along with intramolecular stabilization via B–N or B–O interactions are likely to play roles.[24,38,39] The pK_a value of the